

Maximum entropy theory and the rapid relaxation of three-dimensional quasi-geostrophic turbulence

David A. Schecter*

Advanced Study Program, National Center for Atmospheric Research, P.O. Box 3000, Boulder, Colorado 80307, USA

(Received 17 July 2002; revised manuscript received 29 July 2003; published 31 December 2003)

Turbulent flow in a rapidly rotating stably stratified fluid (quasi-geostrophic turbulence) commonly decays toward a stable pattern of large-scale jets or vortices. A formula for the most probable three-dimensional end state, the maximum entropy state (MES), is derived using a form of Lynden-Bell statistical mechanics. The MES is determined by a set of integral invariants, including energy, as opposed to a complete description of the initial condition. A computed MES qualitatively resembles the quasistationary end state of a numerical simulation that is initialized with red noise, and relaxes for a time on the order of 100 (initial) eddy turnovers. However, the potential enstrophy of the end state, obtained from a coarsened potential vorticity distribution, exceeds that of the MES by nearly a factor of 2. The estimated errors for both theory and simulation do not account for the discrepancy. This suggests that the MES, if ever realized, requires a much longer time scale to fully develop.

DOI: 10.1103/PhysRevE.68.066309

PACS number(s): 47.27.Jv, 05.20.Jj, 47.15.Ki, 47.55.Hd

I. INTRODUCTION

Quasi-geostrophic (QG) turbulence loosely refers to chaotic motions within a rapidly rotating stably stratified fluid, in particular, an atmosphere or ocean [1]. It is well known that unforced QG turbulence can decay by coalescence of small-scale eddies into large-scale stationary jets or vortices. This paper outlines a theory for the most probable three-dimensional (3D) end state, based on the statistical mechanics of incompressible potential vorticity parcels. In addition, the theoretical end state is compared to that of a numerical simulation.

More precisely, this paper examines the inviscid decay of planetary turbulence that is characterized by small Rossby and Froude numbers,

$$\text{Ro} \equiv V/fL_h \ll 1, \text{ and } \text{Fr} \equiv V/NL_v \ll 1.$$

Here V , L_h , and L_v are a typical horizontal velocity, horizontal length scale, and vertical length scale. In addition, f is the Coriolis parameter and N is the buoyancy frequency. For simplicity, we use a local approximation, where f and N are constants. A small Rossby number means that the advection time scale is long compared to the planetary rotation period (a pendulum day). A small Froude number indicates that the phase speed of an internal buoyancy wave far exceeds the horizontal flow speed.

As Ro and Fr approach zero, the fluid motion reduces to QG dynamics [2]:

$$\partial_t q + \vec{v} \cdot \nabla q = 0, \quad \vec{v} = \hat{z} \times \nabla \psi, \quad q = \nabla^2 \psi + \partial_{zz} \psi. \quad (1)$$

In these equations, $\nabla \equiv (\partial_x, \partial_y, 0)$ is the horizontal gradient operator, t is the time, and z is the vertical spatial coordinate, multiplied by N/f . At each height z , the potential vorticity q

is advected without changing value. The horizontal velocity \vec{v} is obtained from the cross gradient of the (scaled) dynamical pressure ψ , which acts as a streamfunction. The vertical velocity is much less than $|\vec{v}|$, and does not appear explicitly in Eqs. (1). The dynamics is closed by a Poisson equation, which relates ψ to q , and boundary conditions.

Figure 1 portrays the free decay of QG turbulence. The simulation occurs in a unit cube, with periodic boundary conditions in the horizontal coordinates x and y . At $z=0$ and 1 , $\partial_z \psi = 0$. Past simulations of decaying QG turbulence have employed spectral [3] or contour dynamics [4] algorithms. Here, the flow is evolved using a particle-in-cell (PIC) code [5], which has no explicit viscosity. The PIC code uses roughly 10^7 particles, and a $128 \times 128 \times 65$ x - y - z mesh. Area weighting is used to obtain the mesh values of potential vorticity (PV) from the particle distribution at each height z .

At $t=0$, the flow consists of red noise, truncated at wave number 10π , with mean and root-mean-square PV equal to zero and one, respectively. The ensuing turbulence appears to chaotically rearrange the PV distribution. Some patches of PV completely shear apart, and become lost in a sea of filaments. Others violently merge with those of like-sign. Ultimately, without losing energy, the flow evolves into a quasistationary pair of counterrotating vortices. One striking feature of the evolution (in this example) is barotropization—a transition toward 2D flow. From beginning to end, the ratio of total energy to that of the vertically averaged flow (the barotropic energy) decreases from 11.74 to approximately 1.07. However, the height-dependent integral invariants of QG dynamics, which we will describe shortly, preserve some vertical variation.

It is reasonable to suppose that the turbulence acts to randomly redistribute potential vorticity, with appropriate constraints. Then, we would expect the time-asymptotic state to resemble the most probable random distribution. We will calculate this “maximum entropy state” using Lynden-Bell statistical mechanics [6,7]. The Lynden-Bell approach can incorporate more constraints than classic point-vortex theory

*Present address: Department of Atmospheric Science, Colorado State University, Fort Collins, Colorado 80523.

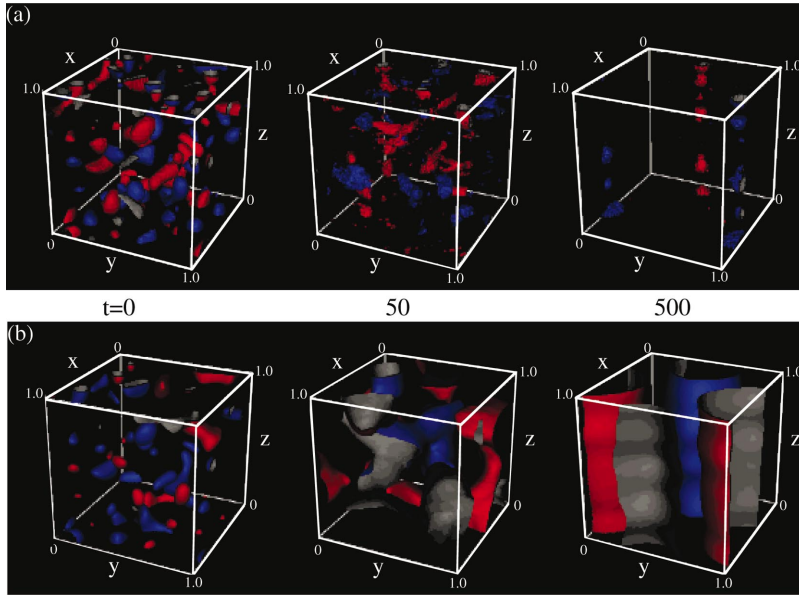


FIG. 1. (Color) Particle-in-cell (PIC) simulation of the relaxation of 3D QG turbulence. (a) PV isosurfaces. Blue, red: $\bar{q}=2.04, -2.04$. (b) Dynamical pressure isosurfaces. Blue, red: $\bar{\psi}=4.48 \times 10^{-3}, -4.48 \times 10^{-3}$. Time is in units of one “eddy turnover,” the inverse of the root-mean-square PV, evaluated on the mesh at $t=0$. Length is in units of the horizontal domain size. *These units are used for all dimensional data.*

[8] or energy-entropy theory [1,9]. It has been applied to ideal 2D hydrodynamics [7], and to low-order layer approximations of oceanic and atmospheric flows [10,11]. This article extends the theory to fully 3D quasi-geostrophic turbulence [12].

For illustrative purposes, we will compare maximum entropy theory to the end-state of Fig. 1. This end state is not time asymptotic; rather, it corresponds to the end of *rapid relaxation*. By $t=500$, various nonconservative flow integrals have slowed their growth or decay rates by at least one order of magnitude (see Appendix B, Fig. 6). Not surprisingly, maximum entropy theory predicts a 3D vortex dipole which is similar to that in Fig. 1. However, the simulated vortex cores are more intense than predicted. The estimated errors for both theory and simulation do not account for the discrepancy. This suggests that the maximum entropy state requires a much longer time scale to fully develop, if it ever will. A more conclusive (and perhaps academic) test of ergodicity would require increasing the time scale and spatial resolution of the simulation by several orders of magnitude. Only then could one ascertain any slow effect of smaller scale turbulence on the domain-size flow. However, such an extensive computational study is beyond the scope of this paper.

II. MAXIMUM ENTROPY STATE OF 3D QUASI-GEOSTROPHIC FLOW

To define a maximum entropy state, we first distinguish between microscopic and macroscopic descriptions of the flow. At the microscopic level, we decompose the PV distribution into a set of infinitesimal fluid elements (microcolumns), which advect the fine-grained PV distribution q in the horizontal plane. We may now imagine a small box centered at a point $\vec{r}=(x,y,z)$ in the fluid. This macrocell contains many microcolumns (Fig. 2). Let $f(\vec{r},\sigma)$, times $d\sigma$, denote the fractional volume of a macrocell that is filled by microcolumns that carry PV in the range $[\sigma,\sigma+d\sigma]$. The sum

over σ of fractional volumes is unity; therefore,

$$F(f;\vec{r}) \equiv \int d\sigma f = 1. \quad (2)$$

The distribution function f fully describes the macrostate of the fluid.

We now define the entropy S of the distribution function f . Let S be the logarithm of the number of ways to arrange the microcolumns, within all of the macrocells, keeping f fixed. By analogy to the entropy of an ideal 2D fluid, derived in Refs. [7], we obtain

$$S(f) = - \int dx dy dz d\sigma f \ln(\sigma_o f) \quad (3)$$

for an ideal 3D QG flow. Equation (3) ignores incidental additive and (positive) multiplicative constants, and σ_o is an arbitrary PV, making the argument of the logarithm dimensionless. The spatial integral covers the entire domain of the flow, and the PV integral extends from minus to positive infinity. These implicit limits of integration occur throughout the article.

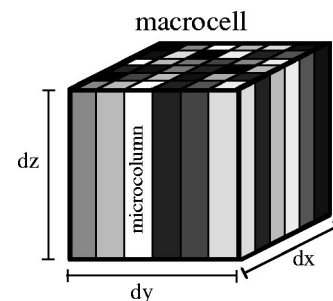


FIG. 2. Cartoon of a macrocell filled with microscopic carriers of “fine-grained” PV (microcolumns). Different shades of gray represent different values of PV.

The statistically most probable distribution function f is that which maximizes S in a subspace that conserves the invariants of QG dynamics. One such invariant is the total horizontal area, at any height z , which is filled by microcolumns with PV in the range $[\sigma, \sigma + d\sigma]$. This quantity is directly proportional to

$$\Gamma(f; z, \sigma) \equiv \int dx dy f. \quad (4)$$

Another crucial invariant is the energy. Up to a constant factor, the energy is given by

$$E(f) \equiv -\frac{1}{2} \int dx dy dz \bar{q} \bar{\psi}, \quad (5)$$

in which

$$\nabla^2 \bar{\psi} + \partial_{zz} \bar{\psi} = \bar{q} \equiv \int d\sigma \sigma f. \quad (6)$$

Here, $\bar{q}(\vec{r})$ is the PV distribution averaged over a macrocell, i.e., the ‘‘coarse-grained’’ PV, and $\bar{\psi}(\vec{r})$ is the corresponding streamfunction. We interpret \bar{q} as the observable PV distribution. Conceivably, the conserved energy E has an additional microscopic component. However, it has been shown elsewhere (for the 2D analog) that this microscopic component is negligible [7]. Henceforth, we will refer to the conserved values of $E(f)$ and $\Gamma(f; z, \sigma)$ as E_o and $\gamma(z, \sigma)$, respectively.

Extrema of S , in the constrained subspace of f , are found by setting equal to zero the first variation of

$$S'(f) \equiv S(f) - \beta E(f) - \int dz d\sigma \mu(z, \sigma) \Gamma(f; z, \sigma) - \int dx dy dz \xi(\vec{r}) F(f; \vec{r}). \quad (7)$$

Here, β , $\mu(z, \sigma)$, and $\xi(\vec{r})$ are Lagrange multipliers. The equation $\delta S' / \delta f = 0$, in combination with Eq. (2), has a solution at $f = f_*$, where

$$f_*(\vec{r}, \sigma) = \frac{e^{\sigma \beta \bar{\psi}_*(\vec{r}) - \mu(z, \sigma)}}{\int d\sigma' e^{\sigma' \beta \bar{\psi}_*(\vec{r}) - \mu(z, \sigma')}}. \quad (8)$$

Here, $\bar{\psi}_*$ is the streamfunction of the macroscopic flow that corresponds to f_* . It satisfies a nonlinear partial differential equation (PDE)

$$\nabla^2 \bar{\psi}_* + \partial_{zz} \bar{\psi}_* = \bar{q}_* \equiv \int d\sigma \sigma f_*, \quad (9)$$

with appropriate boundary conditions. To find f_* , one must vary the Lagrange multipliers, and solve Eq. (9) for $\bar{\psi}_*$, until $E(f_*) = E_o$ and $\Gamma(f_*; z, \sigma) = \gamma(z, \sigma)$.

Let $\bar{q}_o(\vec{r})$ denote the initial form of \bar{q} . Although this function provides a unique value for E_o , it does not provide a unique $\gamma(z, \sigma)$. The values of $\gamma(z, \sigma)$ follow from additional

assumptions. In the following, we will consider two sets of assumptions, and refer to the resulting maximum entropy states as MES1 and MES2.

MES1: One approach is to posit that each microcolumn has one of only three discrete levels of PV: $\sigma_+(z)$, $\sigma_-(z)$, or 0. Unless stated otherwise, we let $\sigma_+(z)$ and $\sigma_-(z)$ equal the maximum and minimum of \bar{q}_o at height z . Smaller amplitudes would prohibit the observed positive and negative extrema of \bar{q}_o .

With only three levels of PV, the area distribution reduces to

$$\gamma(z, \sigma) = \alpha_o(z) \delta(\sigma) + \sum_{j=+,-} \alpha_j(z) \delta(\sigma - \sigma_j(z)), \quad (10)$$

where $\alpha_o = A - \alpha_+ - \alpha_-$, A is the area of the horizontal domain, and δ is a Dirac distribution. If we further assume that the + and - species are initially segregated, then

$$\alpha_{\pm}(z) = \int dx dy H(\pm \bar{q}_o) \bar{q}_o / \sigma_{\pm}, \quad (11)$$

in which $H(\sigma) = 1, 0$ for $\sigma > 0, \sigma < 0$.

In the three-level model, the equation $\Gamma(f_*; z, \sigma) = \gamma(z, \sigma)$ can be satisfied only if

$$e^{-\mu(z, \sigma)} = \delta(\sigma) + \sum_{j=+,-} e^{-\sigma_j(z) \mu_j(z)} \delta(\sigma - \sigma_j(z)). \quad (12)$$

That is, f_* must have the form of f_1 , given by

$$f_1(\vec{r}, \sigma) = \frac{\delta(\sigma) + \delta(\sigma - \sigma_+) e^{\sigma + \Phi_+} + \delta(\sigma - \sigma_-) e^{\sigma - \Phi_-}}{1 + e^{\sigma + \Phi_+} + e^{\sigma - \Phi_-}}, \quad (13)$$

in which $\Phi_{\pm}(\vec{r}) \equiv \beta \bar{\psi}_1(\vec{r}) - \mu_{\pm}(z)$. Here, $\bar{\psi}_1$ is the streamfunction of the macroscopic flow that corresponds to f_1 . From Eqs. (9) and (13), it satisfies the nonlinear PDE

$$\nabla^2 \bar{\psi}_1 + \partial_{zz} \bar{\psi}_1 = \bar{q}_1 = \frac{\sigma_+ e^{\sigma + \Phi_+} + \sigma_- e^{\sigma - \Phi_-}}{1 + e^{\sigma + \Phi_+} + e^{\sigma - \Phi_-}}, \quad (14)$$

with appropriate boundary conditions. The values of the Lagrange multipliers β and $\mu_{\pm}(z)$ are determined by E_o and $\alpha_{\pm}(z)$.

MES2: An alternative approach is to specify $\gamma(z, \sigma)$ indirectly, by giving $\mu(z, \sigma)$ a special form. For example, let us suppose that $\mu(z, \sigma)$ equals $\sigma \hat{\mu}(z)$ in the domain $\sigma_-(z) < \sigma < \sigma_+(z)$, and is otherwise positively infinite. Then, f_* has the form of f_2 , which is given by

$$f_2(\vec{r}, \sigma) = \frac{e^{\sigma \beta \bar{\psi}_2(\vec{r}) - \sigma \hat{\mu}(z)}}{\int_{\sigma_-}^{\sigma_+} d\sigma' e^{\sigma' \beta \bar{\psi}_2(\vec{r}) - \sigma' \hat{\mu}(z)}} \quad (15)$$

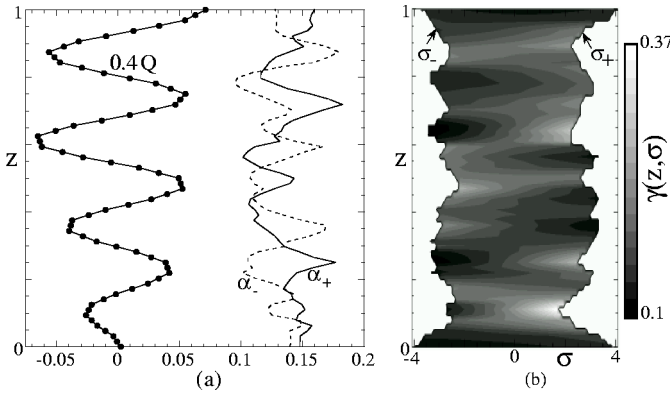


FIG. 3. (a) Height-dependent integrals of the initial PV of a PIC simulation (Fig. 1). These integrals are used with the energy $E_o = 8.5 \times 10^{-4}$ to calculate MES1 and MES2. (Dots on the Q -curve show the discrete heights of the simulation.) (b) Implicit $\gamma(z, \sigma)$ for MES2. Solid black curves indicate the borders of the PV domain $\sigma_-(z) < \sigma < \sigma_+(z)$.

for $\sigma_-(z) < \sigma < \sigma_+(z)$, and is zero otherwise. In Eq. (15), $\bar{\psi}_2$ is the streamfunction of the macroscopic flow that corresponds to f_2 . From Eqs. (9) and (15), it satisfies the nonlinear PDE

$$\nabla^2 \bar{\psi}_2 + \partial_{zz} \bar{\psi}_2 = \bar{q}_2 = -\frac{1}{\Phi} + \frac{\sigma_+ e^{\sigma_+ \Phi} - \sigma_- e^{\sigma_- \Phi}}{e^{\sigma_+ \Phi} - e^{\sigma_- \Phi}}, \quad (16)$$

with appropriate boundary conditions. Here, $\Phi(\vec{r}) \equiv \beta \bar{\psi}_2(\vec{r}) - \hat{\mu}(z)$. The Lagrange multipliers $\hat{\mu}(z)$ and β are determined from \bar{q}_o by the constraints

$$\int dx dy \bar{q}_2 = \int dx dy \bar{q}_o \equiv Q(z) \quad (17)$$

and $E(f_2) = E_o$. The values of $\gamma(z, \sigma)$ implied by this solution are given by $\Gamma(f_2; z, \sigma)$.

III. COMPARISON OF MAXIMUM ENTROPY THEORY TO THE END STATE OF A SIMULATION

We now return to the PIC simulation of Fig. 1, which exemplifies the rapid relaxation of QG turbulence to a quasi-stationary state. To reiterate, during this simulation, decaying turbulence appears to randomly redistribute PV. Accordingly, one may expect the end state of the simulation to resemble a maximum entropy state (MES). The following examines the merits and faults of this hypothesis.

To calculate the MES in part requires that we specify the area distribution $\gamma(z, \sigma)$. In practice, we must approximate γ . We have discussed two methods for doing so, which produce MES1 and MES2 (see Sec. II). For MES1, we obtain γ directly from the integrals $\alpha_{\pm}(z)$ [Eq. (11)]. For MES2, we obtain γ indirectly from the integral $Q(z)$ [Eq. (17)]. Figure 3(a) plots α_{\pm} and Q for the PIC simulation of Fig. 1.

Appendix A describes iterative schemes for computing both MES1 and MES2, given the parameters that appear in Fig. 3. Figure 4 (far right) juxtaposes the resulting PV distributions \bar{q}_1 and \bar{q}_2 . The top, middle, and bottom rows show

contour plots of the x -averaged, y -averaged, and z -averaged PV, respectively. Both MES1 and MES2 predict two vertically aligned columns of opposite PV. The columns comprise lenticular segments. The segments are centered at heights where $Q(z)$ is positively or negatively peaked.

The contour plots show that MES1 and MES2 hardly differ, despite distinct assumptions for $\gamma(z, \sigma)$ [Eq. (10) and Fig. 3(b), respectively]. In both cases, the ratio of total energy to barotropic energy is in the range 1.03 ± 0.01 . In both cases, the potential enstrophy, normalized to the initial value of the simulation, is in the range 0.084 ± 0.001 . The reader may consult Appendix B for the specific definitions of barotropic energy (B1) and potential enstrophy (B2) used here. To further examine theoretical uncertainty, we increased the parameters $\sigma_{\pm}(z)$ of MES1 and MES2 by two orders of magnitude from the values that are shown in Fig. 3(b). The measures of MES1 and MES2 did not change beyond the errors given above.

Figure 4 also shows the final state ($t=500$) of the PIC simulation. Evidently, the simulated end state of rapid relaxation agrees qualitatively with both MES1 and MES2. Furthermore, its ratio of total energy to barotropic energy, 1.07 ± 0.03 , is only slightly greater than predicted. However, the simulated vortex cores have PV levels that are appreciably higher than maximum entropy theory would foretell. This fact is reflected by a normalized potential enstrophy of 0.14 ± 0.02 , which exceeds theory by almost a factor of two, with a strong degree of certainty. Appendix B shows that the discrepancy is not an artifact of the PIC method (see Figs. 5 and 6). Appendix B also explains the estimated error bars for the simulation.

Our 3D result is similar to many past studies of 2D rapid relaxation [13]. Maximum entropy theory seems qualitatively accurate, but quantitatively imprecise. One possible reason for the discrepancy is that violent mergers are unable to efficiently redistribute PV within the cores of the participant vortices [14]. Another possibility is that the maximum entropy state requires a much longer time scale to fully develop. As explained in the Introduction, testing ergodicity beyond rapid relaxation would require vast computational resources, and is not pursued here.

Of note, some studies have actually challenged the qualitative accuracy of 2D maximum entropy theory, over the time scale of rapid relaxation. In a special parameter regime, decaying 2D turbulence seems to freeze due to the spontaneous formation of a vortex crystal equilibrium [15]. Such “crystals” may contain dozens of unmerged vortices. To the author’s knowledge, the parameter regime for this to occur in 3D QG turbulence is yet to be explored.

ACKNOWLEDGMENTS

The author thanks Professor D.H.E. Dubin, Professor B.F. Farrell, Dr. D.Z. Jin and Professor M.T. Montgomery for helpful comments on this research. The author also thanks Dr. J. Tribbia for providing his spectral-grid simulation for the error analysis in Appendix B. This work was done primarily at the National Center for Atmospheric Research, which is funded by the National Science Foundation. Revisions were made under the financial support of the Department of Earth and Planetary Sciences, Harvard University.

066309-5

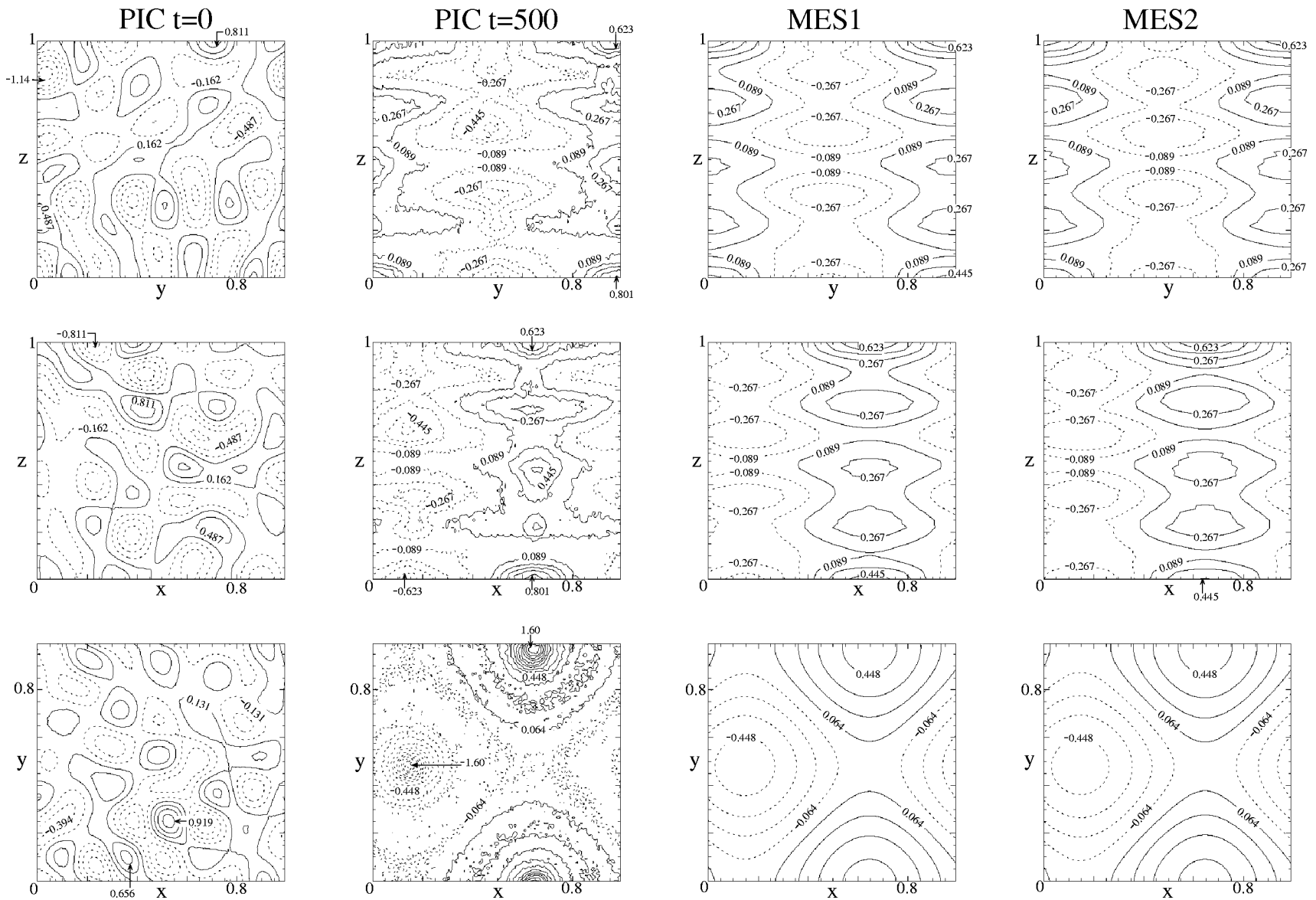


FIG. 4. The end state ($t=500$) of decaying turbulence in the PIC simulation compares favorably to maximum entropy theory. Top: x -averaged PV distributions. Middle: y -averaged PV distributions. Bottom: z -averaged PV distributions. The contours are evenly spaced in PV. The spacings at $t=0$ and at $t=500$ differ. Solid (dashed) contours indicate positive (negative) PV levels, which increase (decrease) monotonically from the perimeter to the interior of a closed region.

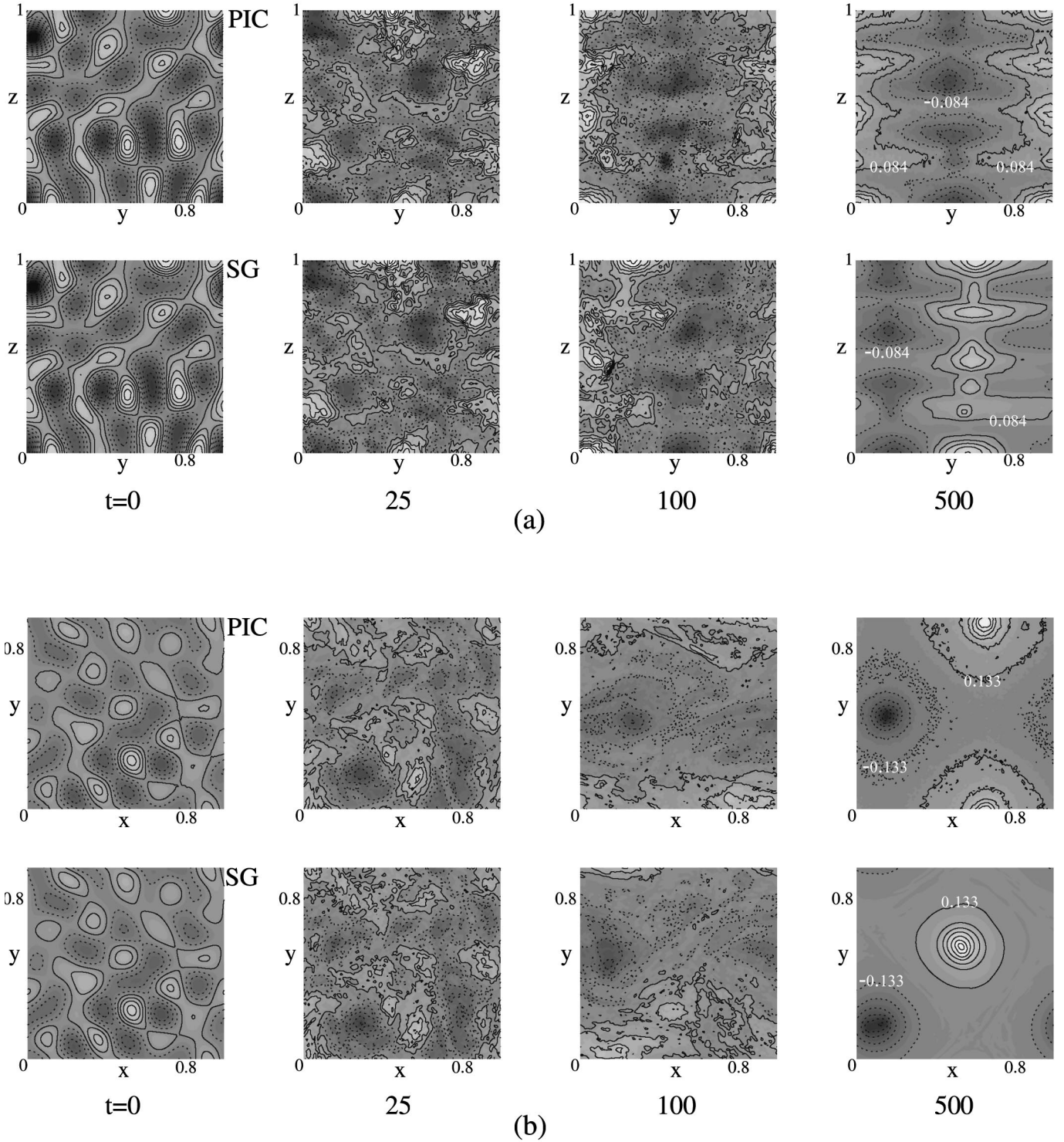


FIG. 5. Evolution of potential vorticity in PIC and SG simulations of comparable resolution: (a) x -averaged PV distributions and (b) z -averaged PV distributions. The contours are evenly spaced in PV, by amounts shown at the far right ($t=500$). This spacing differs from Fig. 4. Lighter (darker) shades represent greater (lesser) values of PV.

APPENDIX A

This appendix describes the iterative schemes that were used to find MES1 and MES2. Both algorithms have the generic form that has been shown, in the context of 2D hydrodynamics, to produce a maximum entropy state [16].

MES1: Let $f_1^k(\vec{r}, \sigma)$, β^k , and $\mu_{\pm}^k(z)$ denote the estimates

of f_1 and the Lagrange multipliers at iteration k . Their values at iteration $k+1$ are solutions to

$$f_1^{k+1} = \frac{\delta(\sigma) + \delta(\sigma - \sigma_+)e^{\sigma_+ \Phi_+^{k+1}} + \delta(\sigma - \sigma_-)e^{\sigma_- \Phi_-^{k+1}}}{1 + e^{\sigma_+ \Phi_+^{k+1}} + e^{\sigma_- \Phi_-^{k+1}}}, \tag{A1a}$$

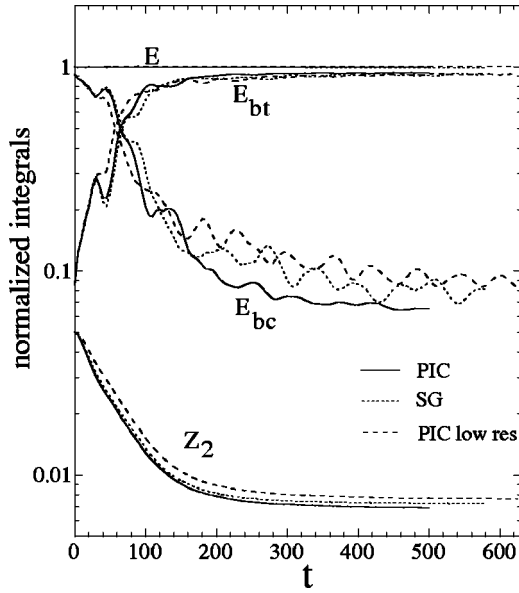


FIG. 6. Evolution of energy and potential enstrophy integrals. The energy integrals are normalized to the initial value of E . Z_2 is divided by 20 times its initial value. Solid curves: “high” resolution PIC simulation. Dotted curves: high resolution SG simulation. Dashed curves: “low” resolution PIC simulation. All simulations are described in the text.

$$\int dx dy \frac{e^{\sigma_{\pm}\Phi_{\pm}^{k+1}}}{1 + e^{\sigma_{+}\Phi_{+}^{k+1}} + e^{\sigma_{-}\Phi_{-}^{k+1}}} = \alpha_{\pm}(z), \quad (\text{A1b})$$

$$- \int dx dy dz \bar{q}_1^{k+1} \bar{\psi}_1^k = E_o + E(f_1^k), \quad (\text{A1c})$$

in which $\Phi_{\pm}^{k+1}(\vec{r}) \equiv \beta^{k+1} \bar{\psi}_1^k(\vec{r}) - \mu_{\pm}^{k+1}(z)$ and $\nabla^2 \bar{\psi}_1^k + \partial_{zz} \bar{\psi}_1^k = \bar{q}_1^k = \int d\sigma \sigma f_1^k$. In practice, (A1b) represents $2N_z$ equations, in which N_z is the number of discrete values for z . Equations (A1b) and (A1c) may be solved for the Lagrange multipliers using Broyden’s method [17].

Sequence (A1) requires a seed f_1^0 . This seed will have the form

$$f_1^0 = \eta_0(\vec{r}) \delta(\sigma) + \eta_+(\vec{r}) \delta(\sigma - \sigma_+(z)) + \eta_-(\vec{r}) \delta(\sigma - \sigma_-(z)),$$

in which $\eta_0 = 1 - \eta_+ - \eta_-$. For this paper, $\eta_{\pm} = H(\pm \bar{q}^0) \bar{q}^0 / \sigma_{\pm}$, in which $\bar{q}^0(\vec{r})$ resembles the simulated coarse-grained PV distribution at $t=0, 50$, or 500 . All three sequences converged to the same state, up to arbitrary horizontal translations. The sequences were stopped when $|E(f^k) - E_o|/E_o \leq 10^{-5}$. The ultimate values of the Lagrange multipliers satisfied $\beta = -17.6$ and $0.41 < |\mu_{\pm}(z)| < 0.89$.

MES2: Let $\bar{q}_2^k(\vec{r})$, β^k , and $\hat{\mu}^k(z)$ denote the estimates of \bar{q}_2 , and the Lagrange multipliers at iteration k . Their values at iteration $k+1$ are solutions to

$$\bar{q}_2^{k+1} = - \frac{1}{\Phi^{k+1}} + \frac{\sigma_+ e^{\sigma_+ \Phi^{k+1}} - \sigma_- e^{\sigma_- \Phi^{k+1}}}{e^{\sigma_+ \Phi^{k+1}} - e^{\sigma_- \Phi^{k+1}}}, \quad (\text{A2a})$$

$$\int dx dy \bar{q}_2^{k+1} = Q(z), \quad (\text{A2b})$$

$$- \int dx dy dz \bar{q}_2^{k+1} \bar{\psi}_2^k = E_o + E(f_2^k), \quad (\text{A2c})$$

in which $\Phi^{k+1}(\vec{r}) \equiv \beta^{k+1} \bar{\psi}_2^k(\vec{r}) - \hat{\mu}^{k+1}(z)$ and $\nabla^2 \bar{\psi}_2^k + \partial_{zz} \bar{\psi}_2^k = \bar{q}_2^k$. Note that $E(f_2^k)$ in (A2c) can be viewed as a functional of \bar{q}_2^k alone.

Sequence (A2) requires a seed \bar{q}_2^0 . For this article, \bar{q}_2^0 was chosen to resemble the simulated PV distribution at $t=50$ or 500 . Both sequences converged to the same coarse-grained PV, up to an arbitrary horizontal translation. The sequences were stopped when $|E(f^k) - E_o|/E_o \leq 10^{-6}$. The ultimate values of the Lagrange multipliers satisfied $\beta = -13.9$ and $-0.26 < \hat{\mu}(z) < 0.14$.

In principle, there can be many discrete *local* maximum entropy states. Some local maxima may have a large number of vortices, whereas others, such as zonal jets, may have none. However, there are likely no other vortex-dipole solutions for MES1 and MES2 than those in Fig. 4. This is because the dipoles emerging from the two optimization algorithms, (A1) and (A2), are robust to large changes in the seeds.

APPENDIX B

This appendix addresses the systematic error of the PIC simulation. We first show that a spectral-grid (SG) simulation of comparable resolution produces approximately the same end state, despite possible concerns to the contrary. We then estimate the error of the PIC simulation, by comparing it to one of half its resolution.

Figure 5 compares the evolution of potential vorticity in the PIC and SG simulations. The SG simulation uses a $128 \times 128 \times 65$ grid, two-thirds dealiasing, and hyperviscosity of the form $\nu(\nabla^2 + 4\partial_{zz})^8 \bar{q}$. The coefficient ν was chosen to dissipate the highest wave number spectral components over the time scale $dt=0.05$. The chaotic flows of the PIC and SG simulations start to diverge after $t=25$, due to slightly different discretization errors. Nonetheless, both simulations relax to vortex dipoles, with similar vertical variations, horizontal length scales, and intensities.

Figure 6 demonstrates that the PIC and SG simulations become nearly barotropic at the same rate. One set of curves shows the temporal growth of barotropic energy

$$E_{bt} \equiv - \frac{1}{2} \int dx dy dz \langle \bar{\psi} \rangle_z \langle \bar{q} \rangle_z, \quad (\text{B1})$$

in which $\langle \rangle_z$ denotes the z average. A second set of curves shows the complimentary decay of baroclinic energy $E_{bc} \equiv E - E_{bt}$. Figure 6 also shows that the potential enstrophy

$$Z_2 \equiv \int dx dy dz \bar{q}^2 \quad (\text{B2})$$

exhibits similar decay in the PIC and SG simulations. To evaluate Z_2 numerically, \bar{q} was first coarsened onto a $64 \times 64 \times 33$ x - y - z mesh, using the method of volume weighting. This convention for Z_2 is used throughout the article.

We now estimate the error of the PIC simulation by comparing it to one of lower resolution, which relaxes to a similar vortex dipole. Figure 6 includes curves for a PIC simulation that uses a $64 \times 64 \times 33$ x - y - z mesh, and roughly 2.5×10^6 particles. The final ($t=500$) barotropic energies of the lower and higher resolution (HR) simulations differ by less than 3% of E_{bt}^{HR} . The final values of Z_2 differ by less than 12% of Z_2^{HR} . The error bars for E/E_{bt}^{HR} and Z_2^{HR} in the main text reflect these percentages.

-
- [1] R. Salmon, in *Topics in Ocean Physics*, Proceedings of the International School of Physics “Enrico Fermi,” Course 80, Varenna, 1980, edited by A.R. Osborne and P. Malanotte Rizzoli (North-Holland, Amsterdam, 1982).
- [2] J. Pedlosky, *Geophysical Fluid Dynamics* (Springer-Verlag, New York, 1987); J.C. McWilliams, *J. Atmos. Sci.* **42**, 1773 (1985).
- [3] J.C. McWilliams *et al.*, *Science* **264**, 410 (1994); *J. Fluid Mech.* **401**, 1 (1999).
- [4] D.G. Dritschel and C. Macaskill, *Geophys. Astrophys. Fluid Dyn.* **92**, 233 (2000).
- [5] A. Leonard, *J. Comput. Phys.* **37**, 288 (1980).
- [6] D. Lynden-Bell, *Mon. Not. R. Astron. Soc.* **136**, 101 (1967).
- [7] J. Miller, *Phys. Rev. Lett.* **65**, 2137 (1990); R. Robert and J. Sommeria, *J. Fluid Mech.* **229**, 291 (1991); J. Miller *et al.*, *Phys. Rev. A* **45**, 2328 (1992); for an interesting comparison of point-vortex and 2D Lynden-Bell statistical mechanics, the reader may consult Z. Yin *et al.*, *Phys. Fluids* **15**, 1937 (2003).
- [8] L. Onsager, *Nuovo Cimento, Suppl.* **6**, 279 (1949); G. Joyce and D. Montgomery, *J. Plasma Phys.* **10**, 107 (1973); T.S. Lundgren and Y.B. Pointin, *J. Stat. Phys.* **17**, 323 (1977).
- [9] W.J. Merryfield, *J. Fluid Mech.* **354**, 345 (1998).
- [10] M.T. DiBattista *et al.*, *Geophys. Astrophys. Fluid Dyn.* **89**, 235 (1998); M.T. DiBattista and A.J. Majda, *J. Phys. Oceanogr.* **30**, 1325 (2000); B. Turkington *et al.*, *Proc. Natl. Acad. Sci. U.S.A.* **98**, 12 346 (2001).
- [11] P.B. Weichman and D.M. Petrich, *Phys. Rev. Lett.* **86**, 1761 (2001); P.H. Chavanis and J. Sommeria, *Phys. Rev. E* **65**, 026302 (2002); F. Bouchet and J. Sommeria, *J. Fluid Mech.* **464**, 165 (2002).
- [12] During the review of this manuscript, the author was informed by Professor A.J. Majda that the following dissertation contains a similar theory, which was not compared to simulations in detail: Sang-Yeun Shim, Ph.D. thesis, New York University, 2000.
- [13] X.-P. Huang and C.F. Driscoll, *Phys. Rev. Lett.* **72**, 2187 (1994); D. Marteau *et al.*, *Phys. Rev. E* **51**, 5124 (1995); M.R. Brown, *J. Plasma Phys.* **57**, 203 (1996); P. Chen and M.C. Cross, *Phys. Rev. Lett.* **77**, 4174 (1996); W.H. Schubert *et al.*, *J. Atmos. Sci.* **56**, 1197 (1999); H. Brands *et al.*, *Phys. Fluids* **11**, 3465 (1999).
- [14] J.C. McWilliams *et al.*, *J. Fluid Mech.* **401**, 1 (1999); G.F. Carnevale *et al.*, *Phys. Rev. Lett.* **66**, 2735 (1991).
- [15] K.S. Fine *et al.*, *Phys. Rev. Lett.* **75**, 3277 (1995); D.Z. Jin and D.H.E. Dubin, *ibid.* **80**, 4434 (1998); D.A. Schecter *et al.*, *Phys. Fluids* **11**, 905 (1999); D.Z. Jin and D.H.E. Dubin, *Phys. Rev. Lett.* **84**, 1443 (2000); J.P. Kossin and W.H. Schubert, *J. Atmos. Sci.* **58**, 2196 (2001); Y. Kiwamoto *et al.*, *Phys. Scr. T* **98**, 34 (2002).
- [16] B. Turkington and A. Whitaker, *SIAM J. Sci. Comput. (USA)* **17**, 1414 (1996).
- [17] W.H. Press *et al.*, *Numerical Recipes in C* (Cambridge University Press, Cambridge, 1992).